4-17-2017

Vector radiative transfer model for coupled atmosphere and ocean systems including inelastic sources in ocean waters

Peng Wang Zhai
University of Maryland, Baltimore County

Yongxiang Hu
NASA Langley Research Center

David M. Winker
NASA Langley Research Center

Bryan A. Franz
NASA Goddard Space Flight Center

Jeremy Werdell
NASA Goddard Space Flight Center

See next page for additional authors

Research Article | Vol. 25, No. 8 | 17 Apr 2017 | OPTICS EXPRESS A223

Optics EXPRESS

Vector radiative transfer model for coupled atmosphere and ocean systems including inelastic sources in ocean waters

PENG-WANG ZHAI,[1,*] YONGXIANG HU,[2] DAVID M. WINKER,[2] BRYAN A. FRANZ,[3] JEREMY WERDELL,[3] AND EMMANUEL BOSS[4]

[1]*Department of Physics, University of Maryland Baltimore County, Baltimore, MD, 21250, USA*
[2]*MS 475 NASA Langley Research Center, Hampton, VA 23681-2199, USA*
[3]*NASA Goddard Space Flight Center, Code 616, Greenbelt, Maryland 20771, USA*
[4]*School of Marine Sciences, University of Maine, Orono, Maine 04401, USA*
[*]*pwzhai@umbc.edu*

Abstract: Inelastic scattering plays an important role in ocean optics. The main inelastic scattering mechanisms include Raman scattering, fluorescence by colored dissolved organic matter (FDOM), and fluorescence by chlorophyll. This paper reports an implementation of all three inelastic scattering mechanisms in the exact vector radiative transfer model for coupled atmosphere and ocean Systems (CAOS). Simulation shows that FDOM contributes to the water radiation field in the broad visible spectral region, while chlorophyll fluorescence is limited in a narrow band centered at 685 nm. This is consistent with previous findings in the literature. The fluorescence distribution as a function of depth and viewing angle is presented. The impacts of fluorescence to the degree of linear polarization (DoLP) and orientation of the polarization ellipse (OPE) are studied. The DoLP is strongly influenced by inelastic scattering at wavelengths with strong inelastic scattering contribution. The OPE is less affected by inelastic scattering but it has a noticeable impact, in terms of the angular region of positive polarization, in the backward direction. This effect is more apparent for deeper water depth.

OCIS codes: (300.6280) Spectroscopy, fluorescence and luminescence; (290.5860) Scattering, Raman; (010.4450) Oceanic optics; (010.4458) Oceanic scattering; (010.5620) Radiative transfer.

References and links

1. C. D. Mobley, *Light and Water: Radiative Transfer in Natural Waters* (Academic, 1994).
2. G. E. Thomas and K. Stamnes, *Radiative Transfer in the Atmosphere and Ocean* (Cambridge University Press, 1999)
3. Z. Ahmad, and R. S. Fraser, "An iterative radiative transfer code for ocean-atmosphere systems," J. Atmos. Sci. **39**, 656–665 (1982).
4. K. Masuda and T. Takashima, "Computational accuracy of radiation emerging from the ocean surface in the model atmosphere - ocean system," Pap. Met. Geophys. **37**, 1–13 (1986).
5. G. W. Kattawar and C. N. Adams, "Stokes vector calculations of the submarine light field in an atmosphere-ocean with scattering according to a Rayleigh phase matrix: effect of interface refractive index on radiance and polarization," Limnol. Oceanogr. **34**, 1453–1472 (1989).
6. G. W. Kattawar and X. Xu, "Detecting Raman scattering in the ocean by use of polarimetry," Proc. SPIE **2258**, 222–233 (1994).
7. H. H. Tynes, G. W. Kattawar, E. P. Zege, I. L. Katsev, A. S. Prikhach, and L. I. Chaikovskaya, "Monte Carlo and multicomponent approximation methods for vector radiative transfer by use of effective Mueller matrix calculations," Appl. Opt. **40**, 400–412 (2001).
8. M. Chami, R. Santer, and E. Dilligeard, "Radiative transfer model for the computation of radiance and polarization in an ocean-atmosphere system: polarization properties of suspended matter for remote sensing," Appl. Opt. **40**, 2398–2416 (2001).
9. J. Chowdhary, B. Cairns, and L. D. Travis, "Contribution of water-leaving radiances to multiangle, multispectral polarimetric observations over the open ocean: bio-optical model results for case 1 waters," Appl. Opt. **45**, 5542–5567 (2006).
10. R. J. D. Spurr, "LIDORT and VLIDORT. Linearized pseudo-spherical scalar and vector discrete ordinate radiative transfer models for use in remote sensing retrieval problems," Light Scattering Rev. **3**, 229–271 (2008).
11. P. Zhai, Y. Hu, C. R. Trepte, and P. L. Lucker, "A vector radiative transfer model for coupled atmosphere and ocean systems based on successive order of scattering method," Opt. Express **17**, 2057–2079 (2009).

#281483 https://doi.org/10.1364/OE.25.00A223
Journal © 2017 Received 29 Nov 2016; revised 30 Jan 2017; accepted 2 Feb 2017; published 3 Mar 2017

12. P. Zhai, Y. Hu, J. Chowdhary, C. R. Trepte, P. L. Lucker, and D. B. Josset, "A vector radiative transfer model for coupled atmosphere and ocean systems with a rough interface," J. Quant. Spectrosc. Radiat. Transfer **111**, 1025–1040 (2010).
13. A. Hollstein and J. Fischer. "Radiative Transfer Solutions for Coupled Atmosphere Ocean Systems Using the Matrix Operator Technique," J. Quant. Spectrosc. Radiat. Transfer **113**, 536–548 (2012)
14. M. Chami, B. Lafrance, B. Fougnie, J. Chowdhary, T. Harmel, and F. Waquet, "OSOAA: a vector radiative transfer model of coupled atmosphere-ocean system for a rough sea surface application to the estimates of the directional variations of the water leaving reflectance to better process multi-angular satellite sensors data over the ocean," Opt. Express **23**, 27829–27852 (2015).
15. F. Xu, O. Dubovik, P. Zhai, D. J. Diner, O.V. Kalashnikova, F. C. Seidel, P. Litvinov, A. Bovchaliuk, M. J. Garay, G. van Harten, and A. B. Davis, "Joint retrieval of aerosol and water-leaving radiance from multispectral, multiangular and polarimetric measurements over ocean," Atmos. Meas. Tech. **9**, 2877–2907 (2016).
16. T. Nakajima and M. Tanaka, "Effect of wind-generated waves on the transfer of solar radiation in the atmosphere-ocean system," J. Quant. Spectrosc. Radiat. Transfer **29**, 521–537 (1983).
17. J. Fischer and H. Grassl, "Radiative transfer in an atmosphere-ocean system: an azimuthally dependent matrix operator approach," Appl. Opt. **23**, 1032–1039 (1984).
18. C. D. Mobley, B. Gentili, H. R. Gordon, Z. Jin, G. W. Kattawar, A. Morel, P. Reinersman, K. Stamnes, and R. H. Stavn, "Comparison of numerical models for computing underwater light fields," Appl. Opt. **32**, 7484–7504 (1993).
19. Z. Jin, T. P. Charlock, K. Rutledge, K. Stamnes, and Y. Wang, "Analytical solution of radiative transfer in the coupled atmosphere–ocean system with a rough surface," Appl. Opt. **45**, 7443–7455 (2006).
20. C. Cox and W. Munk, "Measurement of the roughness of the sea surface from photographs of the suns glitter," J. Opt. Soc. Am. **44**, 838–850 (1954).
21. C. D. Mobley, "Polarized reflectance and transmittance properties of windblown sea surfaces," Appl. Opt. **54**, 4828–4849 (2015).
22. M. Hieronymi, "Polarized reflectance and transmittance distribution functions of the ocean surface," Opt. Express **24**, A1045–A1068 (2016)
23. R. Foster and A. Gilerson, "Polarized transfer functions of the ocean surface for above-surface determination of the vector submarine light field," Appl. Opt. **55**, 9476–9494 (2016)
24. G. E. Walrafen, "Raman spectral studies of effects of temperature on water structure," J. Chem. Phys. **47**, 114–126 (1967).
25. S. Sugihara, M. Kishino, and N. Okami, "Contribution of Raman scattering to upward irradiance in the sea," J. Oceanogr. Soc. Jpn. **40**, 397–404 (1984).
26. R. H. Stavn and A. D. Weidemann, "Optical modeling of clear ocean light fields: Raman scattering effects," Appl. Opt. **27**, 4002–4011 (1988).
27. B. R. Marshall and R. C. Smith, "Raman scattering and in- water ocean optical properties," Appl. Opt. **29**, 71–84 (1990).
28. Y. Ge, K. J. Voss, and H. R. Gordon, "In situ measurements of inelastic scattering in Monterey Bay using solar Fraunhofer lines," J. Geophys. Res. **100**, 13227–13236 (1995).
29. K. J. Waters, "Effects of Raman scattering on water-leaving radiance," J. Geophys. Res. **100**, 13151–13161 (1995).
30. C. M. Hu and K. J. Voss, "In situ measurements of Raman scattering in clear ocean water," Appl. Opt. **36**, 6962–6967 (1997).
31. J. S. Bartlett, K. J. Voss, S. Sathyendranath, and A. Vodacek, "Raman scattering by pure water and seawater," Appl. Opt. **37**, 3324–3332 (1998).
32. H. R. Gordon, "Contribution of Raman scattering to water-leaving radiance: a reexamination," Appl. Opt. **38**, 3166–3174 (1999).
33. H. R. Gordon, M. R. Lewis, S. D. McLean, M. S. Twardowski, S. A. Freeman, K. J. Voss, and G. C. Boynton, "Spectra of particulate backscattering in natural waters," Opt. Express **17**, 16192–16208 (2009).
34. T. K. Westberry, E. Boss, and Z.-P. Lee, "Influence of Raman scattering on ocean color inversion models," Appl. Opt. **52**, 5552–5561 (2013).
35. H. R. Gordon, "The diffuse reflectance of the ocean: The theory of its augmentation by chlorophyll a fluorescence at 685 nm," Appl. Opt. **18**, 1161–1166 (1979).
36. R. W. Preisendorfer and C. D. Mobley, "Theory of fluorescent irradiance fields in natural waters," J. Geophys. Res. **93D**, 10831–10855 (1988).
37. A. M. Kouassi, R. G. Zika, and J. M. C. Plane, "Light-induced alteration of the photophysical properties of dissolved organic matter in sea water," Neth. J. Sea Res. **27**, 33–41 (1990).
38. S. A. Green and N. V. Blough, "Optical absorption and fluorescence properties of chromophoric dissolved organic matter in natural waters," Limnol. Oceanogr. **39**, 1903–1916 (1994)
39. A. Vodacek, N. V. Blough, M. D. DeGrandpre, E. T. Peltzer, and R. K. Nelson, "Seasonal variation of CDOM and DOC in the Middle Atlantic Bight: terrestrial inputs and photooxidation," Limnol. Oceanogr. **42**, 674–686 (1997)
40. L. Li, D. Stramski, and R. A. Reynolds, "Effects of inelastic radiative processes on the determination of water-leaving spectral radiance from extrapolation of underwater near-surface measurements," Appl. Opt. **55**, 7050-7067 (2016)
41. D. Pozdiakov and H. Grassl, *Color of Inland and Coastal Waters: A Methodology for its Interpretation* (Springer-Praxis, 2003)

Optics EXPRESS

42. J. Vigneshwaran, P. Shanmugam, and E. A. Gokul, "Simulating the effects of inelastic scattering on upwelling radiance in coastal and inland waters: implications for hyperspectral remote sensing," Current Sci. **108**, 903–914, (2015).
43. M. J. Behrenfeld, T. K. Westberry, E. S. Boss, R. T. O'Malley, D. A. Siegel, J. D. Wiggert, B. A. Franz, C. R. McClain, G. C. Feldman, S. C. Doney, J. K. Moore, G. Dall'Olmo, A. J. Milligan, I. Lima, and N. Mahowald, "Satellite-detected fluorescence reveals global physiology of ocean phytoplankton," Biogeosciences **6**, 779–794, (2009).
44. G. W. Kattawar and X. Xu, "Filling in of Fraunhofer lines in the ocean by Raman scattering," Appl. Opt. **31**, 6491–6500 (1992).
45. Y. T. Ge, H. R. Gordon, and K. J. Voss, "Simulation of inelastic scattering contributions to the irradiance field in the ocean: variation in Fraunhofer line depths," Appl. Opt. **32**, 4028–4036 (1993).
46. M. Schroeder, H. Barth, and R. Reuter, "Effect of inelastic scattering on underwater daylight in the ocean: model evaluation, validation, and first results," Appl. Opt. **42**, 4244–4260 (2003).
47. P. Zhai, Y. Hu, D. M. Winker, B. A. Franz, and E. Boss, "Contribution of Raman scattering to polarized radiation field in ocean waters," Opt. Express **23**, 23582–23596 (2015).
48. A. Wolanin, V. Rozanov, T. Dinter, and A. Bracher, "Detecting CDOM fluorescence using high spectrally resolved satellite data: a model study," in *Towards an Interdisciplinary Approach in Earth System Science*, G. Lohmann, H. Meggers, V. Unnithan, D. Wolf-Gladrow, J. Notholt, and A. Bracher, eds. (Springer Earth System Sciences, 2015).
49. S. K. Hawes, C. K. Carder, and G. R. Harvey, "Quantum fluorescence efficiencies of fulvic and humic acids: effects on ocean color and fluorometric detection," Proc. SPIE **1750**, 212–223 (1992).
50. J. R. Morrison, "In situ determination of the quantum yield of phytoplankton chlorophyll a fluorescence: A simple algorithm, observations, and a model," Limnol. Oceanogr. **48**, 618–631 (2003).
51. P. Zhai, Y. Hu, C. R. Trepte, D. M. Winker, P. L. Lucker, Z. Lee, and D. B. Josset, "Uncertainty in the bidirectional reflectance model for oceanic waters," Appl. Opt. **54**, 4061–4069 (2015).
52. R. M. Pope and E. S. Fry, "Absorption spectrum (380–700 nm) of pure water. II Integrating measurements," Appl Opt. **36**, 8710–8723 (1997).
53. X. Zhang and L. Hu, "Scattering by pure seawater at high salinity," Opt. Express **17**, 12685–12691 (2009).
54. K. J. Voss, "A spectral model of the beam attenuation coefficient in the ocean and coastal areas," Limnol. Oceanogr. **37**, 501–509 (1992).
55. IOCCG Ocean Color Algorithm Working Group, "Models, parameters, and approaches that used to generate wide range of absorption and backscattering spectra," (2003).
56. A. Bricaud, A. Morel, M. Babin, K. Allali, and H. Claustre, "Variations of light absorption by suspended particles with chlorophyll a concentration in oceanic (case 1) waters: analysis and implications for bio-optical models," J Geophys. Res. **103**, 31033–31044 (1998).
57. J. Wei and Z. Lee, "Retrieval of phytoplankton and colored detrital matter absorption coefficients with remote sensing reflectance in an ultraviolet band," Appl. Opt. **54**, 636–649 (2015)
58. A. Bricaud, A. Morel, and L. Prieur, "Absorption by dissolved organic matter of the sea (yellow substance) in the UV and visible domains," Limnol. Oceanogr. **26**, 43–53, (1981).
59. A. Morel and S. Maritorena, "Bio-optical properties of oceanic waters: a reappraisal," J Geophys. Res. **106**, 7163–7180 (2001).
60. A. Morel and B. Gentili, "A simple band ratio technique to quantify the colored dissolved and detrital organic material from ocean color remotely sensed data," Rem. Sens. Environ. **113**, 998–1011 (2009).
61. Y. Huot, A. Morel, M. S. Twardowski, D. Stramski, and R. A. Reynolds, "Particle optical backscattering along a chlorophyll gradient in the upper layer of the eastern South Pacific Ocean," Biogeosciences **5**, 495–507 (2008).
62. G. Fourier and J. L. Forand, "Analytic phase function for ocean water," Proc. SPIE **2258**, 194–201 (1994).
63. G. Fournier and M. Jonasz, "Computer-based underwater imaging analysis," Proc. SPIE **3761**, 62–70 (1999).
64. C. D. Mobley, L. K. Sundman, and E. Boss, "Phase function effects on oceanic light fields," Appl. Opt. **41**, 1035–1050 (2002).
65. K. J. Voss and E. S. Fry, "Measurement of the Mueller matrix for ocean water," Appl Opt. **23**, 4427–4439 (1984).
66. A. A. Kokhanovsky, "Parameterization of the Mueller matrix of oceanic waters," J. Geophys. Res. **108**, 3175 (2003).
67. Committee on Extension to the Standard Atmosphere, *U. S. Standard Atmosphere*, (U.S. Government Printing Office, Washington D.C. 1976).
68. C. Tomasi, V. Vitale, B. Petkov, A. Lupi, and A. Cacciari, "Improved algorithm for calculations of Rayleigh-scattering optical depth in standard atmospheres," Appl. Opt. **44**, 3320–3341 (2005).
69. J. E. Hansen and L. D. Travis, "Light scattering in planetary atmospheres," Space Sci. Rev. **16**, 527–610 (1974).
70. E. P. Shettle and R. W. Fenn, "Models for the aerosols of the lower atmosphere and the effects of humidity variations on their optical properties," AFGL-TR-79-0214 U.S. Air Force Geophysics Laboratory, Hanscom Air Force Base, Mass., 1979 .
71. N. Braslau and J. V. Dave, "Effect of aerosols on the transfer of solar energy through realistic model atmospheres. Part I: non-absorbing aerosols," J. Appl. Meteor. **12**, 601–615 (1973).
72. G. Thuillier, M. Herse, S. Labs, T. Foujols, W. Peetermans, D. Gillotay, P.C. Simon, and H. Mandel, "The solar spectral irradiance from 200 to 2400 nm as measured by SOLSPEC Spectrometer from the ATLAS 123 and EURECA missions," Solar Phys. **214**, 1–22 (2003).

Optics EXPRESS

73. J. Uitz, H. Claustre, A. Morel, and S. B. Hooker, "Vertical distribution of phytoplankton communities in open ocean: An assessment based on surface chlorophyll," J. Geophys. Res. **111**, C08005 (2006).
74. A. Morel and J. F. Berthon, "Surface pigments, algal biomass profiles, and potential production of the euphotic layer: Relationships reinvestigated in view of remote-sensing applications," Limnol. Oceanogr. **34**, 1545–1562 (1989).
75. P. Eriksson, S. A. Buehler, C. P. Davis, C. Emde, and O. Lemke, "ARTS, the atmospheric radiative transfer simulator, Version 2," J. Quant. Spectrosc. Radiat. Transfer **112**, 1551–1558 (2011).
76. L.S. Rothman, I.E. Gordon, Y. Babikov, A. Barbe, D. Chris Benner, P.F. Bernath, M. Birk, L. Bizzocchi, V. Boudon, L.R. Brown, A. Campargue, K. Chance, E.A. Cohen, L.H. Coudert, V.M. Devi, B.J. Drouin, A. Fayt, J.-M. Flaud, R.R. Gamache, J.J. Harrison, J.-M. Hartmann, C. Hill, J.T. Hodges, D. Jacquemart, A. Jolly, J. Lamouroux, R.J. Le Roy, G. Li, D.A. Long, O.M. Lyulin, C.J. Mackie, S.T. Massie, S. Mikhailenko, H.S.P. Müller, O.V. Naumenko, A.V. Nikitin, J. Orphal, V. Perevalov, A. Perrin, E.R. Polovtseva, C. Richard, M.A.H. Smith, E. Starikova, K. Sung, S. Tashkun, J. Tennyson, G.C. Toon, Vl.G. Tyuterev, and G. Wagner, "The HITRAN2012 molecular spectroscopic database," J. Quant. Spectrosc. Radiat. Transfer **130**, 4–50 (2013).
77. A. Ibrahim, A. Gilerson, T. Harmel, A. Tonizzo, J. Chowdhary, and S. Ahmed, "The relationship between upwelling underwater polarization and attenuation/absorption ratio," Opt. Express **20**, 25662–25680 (2012)

1. Introduction

Radiative transfer for coupled atmosphere and ocean systems (CAOS) combines atmospheric radiation and ocean optics in a unified theoretical frame [1, 2]. Exact radiative transfer solutions preserve the polarization nature of the radiation, which is generally referred to as vector radiative transfer [3–15]. If the polarization nature of the radiation is ignored, the vector radiative transfer is reduced to the scalar radiative transfer, which only solves the approximated intensity of the radiation [16–19]. Sea surface roughness is normally parameterized in terms of wind speed at 10 meters above ocean surface [20]. Recently new developments have been made to study the reflection and transmission properties of rough surfaces with different Fourier spectra, sea swell, and diffuse incident light fields [21–23].

Only a few models have considered the contribution from inelastic scattering, in which radiation changes wavelengths [1, 6]. However, inelastic scattering is recognized to be an important source in ocean optics. This includes Raman scattering [24–34] and fluorescence [35–39]. These inelastic sources have been considered in the commercial software Hydrolight, which deals with scalar radiative transfer for ocean waters [1]. Li et al. studied the impacts of inelastic scattering to extrapolating water leaving radiance from near surface measurements [40]. Approximate semi-analytical models have been developed to simulate inelastic scattering [41, 42]. Raman scattering and chlorophyll fluorescence have also been used to better invert the oceanic remote sensing signal to biogeochemical parameters [34, 43]. Progress has been made to incorporate inelastic scattering in exact radiative transfer models for CAOS [44–48].

In this paper we report an exact vector radiative transfer model for CAOS that incorporates both elastic and inelastic scattering processes. The solution is based on the successive order of scattering (SOS) method [11, 12]. Previously the implementation of Raman scattering in the SOS for CAOS has been published [47]. The new addition to the SOS model is the fluorescence by colored dissolved organic matter (FDOM) and chlorophyll fluorescence, which is the main focus of this paper. Our model possesses a unique combination of the following features: 1) full atmosphere and ocean coupling; 2) exact treatment of the polarization; 3) inclusion of all major inelastic scattering mechanisms; 4) formulas based on the SOS method that are efficient and accurate; 5) no approximation on the angular and polarization distribution features of the elastic and inelastic scattering sources.

The FDOM and chlorophyll fluorescence are assumed to be isotropic and non-polarized [1]. However, it is still necessary to incorporate fluorescence in a vector radiative transfer model because the multiple interaction between fluorescence, elastic, and Raman scattering induces polarization. This paper is organized as follows: Sec. 2 presents the generalized vector inelastic radiative transfer equation based on the scalar version in [1]; Sec. 3 outlines the ocean biooptical model used for simulation; Sec. 4 shows the practical simulation procedures and results; Sec. 5

summarizes the main conclusions.

2. Inelastic vector radiative transfer equation

The inelastic vector radiative transfer equation for a plane-parallel system without thermal emission can be written as [1, 32, 47]:

$$\mu \frac{d\mathbf{L}(z,\mu,\phi,\lambda)}{dz} = -c(z,\lambda)\mathbf{L}(z,\mu,\phi,\lambda) + \mathbf{S}(z,\mu_0,\mu,\phi,\lambda) + \mathbf{S}_i(z,\mu_0,\mu,\phi,\lambda), \quad (1)$$

where $\mathbf{L}$=[I, Q, U, V]$^{\mathrm{T}}$ is the Stokes vector and superscript T stands for transpose; $\mathbf{S}$ and $\mathbf{S}_i$ are the elastic and inelastic source terms, respectively; z is the vertical coordinate; $\mu_0 = \cos\theta_0$; $\mu = \cos\theta$; θ_0 and θ are the solar and viewing zenith angles, respectively; ϕ is the viewing azimuth angle; λ is the emission wavelength; c is the extinction coefficient. The inelastic source terms are summation of three mechanisms:

$$\mathbf{S}_i = \mathbf{S}_{\mathrm{R}} + \mathbf{S}_{\mathrm{Y}} + \mathbf{S}_{\mathrm{C}}, \quad (2)$$

where the subscripts R, Y, and C stand for Raman scattering, FDOM, and chlorophyll fluorescense, respectively.

The elastic source $\mathbf{S}$ and Raman scattering source $\mathbf{S}_{\mathrm{R}}$ have been described in [47] with the same terminology convention, which we omit here for conciseness. The readers are referred to [47] for a detailed description. Here we focus on $\mathbf{S}_{\mathrm{Y}}$ and $\mathbf{S}_{\mathrm{C}}$ in the theoretical frame of vector radiative transfer:

$$\mathbf{S}_{\mathrm{F}}(z,\mu,\phi,\lambda) = \int_0^{\infty}\int_0^{2\pi}\int_{-1}^{1} b_{\mathrm{F}}(z,\lambda,\lambda_e)\mathbf{P}_{\mathrm{F}}(z,\mu,\phi,\mu',\phi',\lambda,\lambda_e)\cdot\mathbf{L}(z,\mu',\phi',\lambda_e)d\mu' d\phi' d\lambda_e, \quad (3)$$

where the subscript F can be either Y or C, denoting FDOM or chlorophyll; b_{F} is the fluorescence scattering coefficient; and λ_e denotes the excitation wavelength. We assume the fluorescence phase matrix $\mathbf{P}_{\mathrm{F}}$ is isotropic and unpolarized [1]:

$$P_{\mathrm{F},ij} = \begin{cases} 1/(4\pi), & ij = 11, \\ 0, & i \neq 1 \ \ or \ \ j \neq 1. \end{cases} \quad (4)$$

where $P_{\mathrm{F},ij}$ is the ijth matrix element of $\mathbf{P}_{\mathrm{F}}$. The fluorescence scattering coefficient b_{F} can be written as a product of two terms [1]:

$$b_{\mathrm{F}}(z,\lambda,\lambda_e) = a_{\mathrm{F}}(z,\lambda_e) f_{\mathrm{F}}(z,\lambda,\lambda_e), \quad (5)$$

where a_{F} is the absorption coefficient of either colored dissolved organic matter (CDOM) or chlorophyll at excitation wavelength λ_e; and f_{F} is the fluorescence redistribution function [1]:

$$f_{\mathrm{F}}(z,\lambda,\lambda_e) = \eta_{\mathrm{F}}(z,\lambda,\lambda_e)\lambda_e/\lambda, \quad (6)$$

where $\eta_{\mathrm{F}}(z,\lambda,\lambda_e)$ is the spectral fluorescence quantum efficiency function, defined as the ratio of the number of photons emitted at λ per unit wavelength interval and the number of photons absorbed at λ_e. The factor λ_e/λ accounts for energy being proportional to $1/\lambda$ for a photon.

The function η_{F} varies with substance. For FDOM, we replace subscript F with Y, and use the parameterization by Hawes et al. [49]:

$$\eta_{\mathrm{Y}}(\lambda,\lambda_e) = g_{\mathrm{Y}}(\lambda_e)A_0(\lambda_e)\exp\left\{-\left[\frac{1/\lambda - A_1/\lambda_e - B_1}{0.6\,(A_2/\lambda_e + B_2)}\right]^2\right\}, \quad (7)$$

where A_0, A_1, A_2, B_1, and B_2 are parameters that depend on the particular composition of the yellow matter. Hawes et al [49] provided tabulated values of these parameters for four fulvic acid samples: (FA7, FA8, FA9, FA10); and seven humic acid samples: (HA1, HA2, HA3, HA4, HA5, HA6), extracted from ocean waters. In this work we model FDOM using a mixture of 9/10 of FA7 and 1/10 of HA6, which was also assumed in [49]. The symbol g_Y is a dimensionless function, which specifies the range of excitation wavelength within which η_Y is significant:

$$g_Y = \begin{cases} 1, & 310 \le \lambda_e \le 490\text{nm}; \\ 0, & \lambda_e > 490 \quad \text{or} \quad \lambda_e < 310\text{nm}. \end{cases} \tag{8}$$

However, the inherent optical property measurement for wavelengths below 350 nm is less common and difficult to verify. Hereafter the wavelengths λ and λ_e are referred in the unit of nm. We have assumed $g_Y = 0$ for λ_e <350 nm. This can be justified with the strong ozone absorption and decreased solar spectral irradiance in the UV. Green and Blough [38] found that the FDOM fluorescence quantum efficiency is different when FDOM is extracted or still dissolved in water samples. This mitigates the applicability of the data from Hawes et al. [49], which was measured from the FDOM samples extracted from ocean waters. Readers are referred to [38] for a detailed discussion of the measurement of FDOM in natural waters. However, the data in [49] are still the only complete set of data that covers a whole range of excitation and emission wavelengths. We better adopt the approach of [49] in this work to demonstrate our implementation of FDOM fluorescence. When future data are available, they can be easily adopted within the computational package.

The chlorophyll fluorescence quantum efficiency function η_C takes the form of [1]:

$$\eta_C(\lambda, \lambda_e) = \Phi_C(\lambda_e) g_C(\lambda_e) h_C(\lambda), \tag{9}$$

where $\Phi_C(\lambda)$ is the fluorescence quantum yield of chlorophyll:

$$\Phi_C(\lambda_e) = \int_0^\infty \eta_C(\lambda, \lambda_e) d\lambda; \tag{10}$$

the dimensionless function g_C specifies the spectral range:

$$g_C = \begin{cases} 1, & 370 \le \lambda_e \le 690\text{nm}; \\ 0, & \lambda_e > 690 \quad \text{or} \quad \lambda_e < 370\text{nm}. \end{cases} \tag{11}$$

The emission function $h_C(\lambda)$ is approximated by a Gaussian [1]:

$$h_C(\lambda) = \frac{1}{\sqrt{2\pi}\sigma_C} \exp\left[-\frac{(\lambda - \lambda_{C,0})^2}{2\sigma_C^2} \right], \tag{12}$$

where $\lambda_{C,0}$ =685 nm is the wavelength of maximum emission, and σ_C = 10.6 nm is the standard deviation of the Gaussian.

The quantum yield Φ_C typically ranges between 0.01 and 0.05 , which depends on phytoplankton species, physiological state, and other environmental factors [1]. One mechanism of Φ_C variation is called non-photochemical quenching (NPQ), under which algae reduce Φ_C under large irradiance to protect themselves [43, 50]. The impacts of NPQ to chlorophyll fluorescence is beyond the scope of this study. We used a constant Φ_C=0.02 to show the mean features of chlorophyll fluorescence.

3. Biooptical models of ocean waters

Inelastic scattering simulations need to consider transspectral optical properties, for which a biooptical model for ocean waters is necessary. The set of biooptical models used in [47, 51] are

followed with modifications highlighted below in order to better conform spectral behavior of particle absorption and scattering coefficients. The ocean water is composed of three components: pure ocean water, phytoplankton covariant particles, and absorptive CDOM. The total extinction coefficient $c(\lambda, [\text{Chla}])$ at wavelength λ for a chlorophyll a value [Chla] is assumed to follow:

$$c(\lambda, [\text{Chla}]) = c_w(\lambda) + c_p(\lambda, [\text{Chla}]) + c_\text{Y}(\lambda, [\text{Chla}]), \tag{13}$$

where the subscript w, p, and Y stand for pure sea water, phytoplankton covariant particles, and CDOM, respectively. The extinction coefficient for each component is a sum of the absorption and scattering coefficient [1]:

$$\begin{aligned} c_w(\lambda) &= a_w(\lambda) + b_w(\lambda), \\ c_p(\lambda, [\text{Chla}]) &= a_p(\lambda, [\text{Chla}]) + b_p(\lambda, [\text{Chla}]), \\ c_\text{Y}(\lambda, [\text{Chla}]) &= a_\text{Y}(\lambda, [\text{Chla}]) + b_\text{Y}(\lambda, [\text{Chla}]). \end{aligned} \tag{14}$$

The pure water absorption coefficient a_w are based on data in [52]; and b_w follows: [1,53]:

$$b_w(\lambda) = 0.00193 \cdot (550/\lambda)^{4.32}. \tag{15}$$

The dependence of b_w on salinity and temperature is not considered here.

The extinction coefficient c_p of phytoplankton covariant particles takes the form of [54,55]:

$$\begin{aligned} c_p(\lambda, [\text{Chla}]) &= c_p(550, [\text{Chla}])(550/\lambda)^{n_1}, \\ c_p(550, [\text{Chla}]) &= p_1[\text{Chla}]^{0.57}, \\ n_1 &= -0.4 + \frac{1.6 + 1.2R_1}{1 + [\text{Chla}]^{0.5}}, \end{aligned} \tag{16}$$

where both p_1 and R_1 are numbers that can vary in nature and are in general unknown. In [55], p_1 is modeled as a random number uniformly distributed between 0.06 and 0.6 and R_1 is modeled as a random number uniformly distributed between 0 and 1. In this work we assigned $p_1 = 0.33$ and $R_1 = 0.5$ for the sake of clarity of the simulations. The particle absorption coefficients $a_p([\text{Chla}],\lambda)$ are a function [Chla] and wavelength λ [56]. As noted in [47], the absorption data in [56] covers the wavelength range of 400 nm to 700 nm. In order to evaluate the inelastic source term, a second set of the absorption data is used to expand the spectral range to the UV [57]. The continuity of these two sets of absorption data is assured by scaling the data in [57] to the same value as in [56] at 440 nm. The particle scattering coefficient is simply the difference between c_p and a_p: $b_p = c_p - a_p$.

We assume the scattering coefficient for CDOM $b_\text{Y} = 0$. The CDOM absorption is [55,58–60]:

$$\begin{aligned} a_\text{Y}(\lambda, [\text{Chla}]) &= a_\text{Y}(440, [\text{Chla}]) \cdot \exp(-0.014(\lambda - 440)), \\ a_\text{Y}(440, [\text{Chla}]) &= p_2 \cdot a_p(440, [\text{Chla}]), \\ p_2 &= 0.3 + \frac{5.7 \cdot R_2 \cdot a_p(440, [\text{Chla}])}{0.02 + a_p(440, [\text{Chla}])}. \end{aligned} \tag{17}$$

where R_2 is a random number uniformly distributed between 0 and 1 to account for natural variability as introduced by its original authors. In this paper we assigned $R_2 = 0.5$. It should be noted that the origin of CDOM is from diverse sources including natural and industrial land discharges, and the biological activity averaged over a long period [58]. Consequently, the correlation between CDOM and [Chla] is rather weak for measurements taken from specific time and locations. However, the CDOM and chlorophyll a concentrations averaged over large spatial and time scales do correlate [59,60]. Here we adopt Eq. (17) to reflect this correlation in our model

with the understanding that the correlation may not be applicable to local measurements [55]. In this situation, we could use local measurements of $a_Y(440)$ to replace $a_Y(440, [\text{Chla}])$ in the formulas, with other parts intact.

As an illustration, Fig. 1 shows the single scattering albedo for ocean waters determined from the absorption and scattering properties outlined above for a set of [Chla] values. The spectral shape agrees with the literature [9], which demonstrates the consistency of the bio-optical model employed.

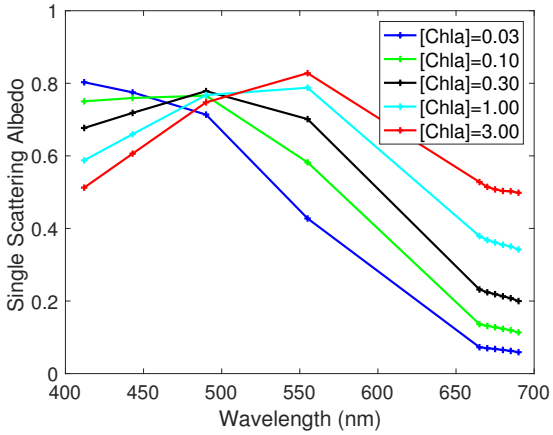

Fig. 1. Single scattering albedo of ocean waters for a set of [Chla] values

The backscattering ratio is defined as $B_{bp} = b_{bp}/b_p$, where b_{bp} is the backscattering coefficient. For phytoplankton covariant particles B_{bp} is [61]:

$$B_{bp}([\text{Chla}]) = 0.002 + 0.01(0.5 - 0.25 \log_{10}[\text{Chla}]). \tag{18}$$

For a specific value of [Chla], Eq. (18) is used to determine B_{bp}. The elastic scattering phase function $P_{11,p}$ for phytoplankton covariant particles is then the Fournier-Forand phase function [62, 63], parameterized based on backscattering ratio [64]. The total ocean scattering phase function is a weighted sum of phytoplankton particle and pure water:

$$P_{11} = (b_p P_{11,p}(\Theta) + b_w P_{11,w}(\Theta))/(b_p + b_w), \tag{19}$$

where $P_{11,w}(\Theta)$ is the pure water phase function [1]; and Θ is the scattering angle. The elastic reduced scattering matrix of the ocean water is a parameterization of measurement by Voss [65, 66]. The main rationale of this choice is that the average measurements [65] represent the reality of a variety of ocean waters. In addition, we wish to preserve the features P_{22}/P_{11} observed in ocean waters, which is quite important in some cases. Note that the use of Mie theory will result in $P_{22}/P_{11} = 1$, which is not observed for ocean waters.

4. Simulations and discussion

Inelastic radiative transfer simulation involves two steps. The first step is to perform a series of elastic radiative transfer calculations at a range of excitation wavelengths that have notable contributions to the inelastic source term $\mathbf{S}_i$. The second step is to gather all the inelastic source terms $\mathbf{S}_i$ and the elastic source $\mathbf{S}$ and perform the radiative transfer simulation at the emission wavelength. Higher order inelastic scattering terms of fluorescence being absorbed and re-emitted are proportional to the higher polynomial order of quantum yields which are assumed negligible

and ignored in this work. The interaction of excitation and emission radiation fields requires an optical model that correlates the single scattering properties at different wavelengths for both the atmosphere and ocean. For the atmosphere, it is assumed to be a mixture of molecules and aerosols. The vertical profile of the molecule number density is determined by the 1976 US standard atmosphere [67]. The molecule scattering optical depth is calculated using the method in [68]. The molecule scattering matrix is the Rayleigh scattering matrix with a depolarization of 0.0284 [69]. The aerosol model is the Maritime aerosol model with relative humidity of 80% [70]. The aerosol optical depth at 550 nm is 0.15. The aerosol vertical distribution follows the average height distribution in [71]. Gas absorption in the atmosphere is not considered, but rather assumed to be removed through atmospheric correction. The Cox-Munk model is used to specify ocean surface roughness based on wind speed [20]. The dependence of ocean roughness on wind direction is neglected. The solar spectral irradiance data are those reported in [72].

The ocean optical properties are determined from the biooptical model in Sec. 3 for specified wavelengths and [Chla] values. The vertical distribution of [Chla] is a generalized Gaussian superposed onto a linearly decreasing background [73]. To enable assigning a full vertical [Chla] profile to a single surface value, we first determine an integrated value over the euphotic zone through [73]:

$$[\text{Chla}]_{Zeu} = A[\text{Chla}]_{\text{surf}}^{B}, \tag{20}$$

where the fitting parameters A and B are provided in Table 4 in [73]. Then the depth of the euphotic layer Z_{eu} is [74]:

$$Z_{eu} = 568.2([\text{Chla}]_{Zeu})^{-0.746}. \tag{21}$$

The depth z and chlorophyll a concentration [Chla] is then rescaled [73]:

$$\begin{aligned} \zeta &= z/Z_{eu}, \\ \overline{[\text{Chla}]}_{Zeu} &= [\text{Chla}]_{Zeu}/Z_{eu}, \\ \chi &= [\text{Chla}]/\overline{[\text{Chla}]}_{Zeu}. \end{aligned} \tag{22}$$

Given the above notations, the rescaled chlorophyll a concentration profile is [73]:

$$\chi(\zeta) = \chi_b - s\zeta + \chi_{max}\exp\{-[(\zeta - \zeta_{max})/\Delta\zeta]^2\}, \tag{23}$$

where χ_b is the rescaled background [Chla] value, s is the linear slope, χ_{max} is the rescaled maximum concentration, ζ_{max} is the depth at which maximum concentration is located; and, $\Delta\zeta$ determines the width of the Gaussian peak. In this study, we have used the following parameters: χ_b = 0.471, s=0.135, χ_{max}=1.572, ζ_{max}=0.969, and $\Delta\zeta$=0.393, which is the tropic class S1 case shown in Table 5 in [73]. The final vertical [Chla] profile is given by:

$$[\text{Chla}](\zeta) = [\text{Chla}]_{\text{surf}}\frac{\chi(\zeta)}{\chi(\zeta = 0)}, \tag{24}$$

so that the vertical chlorophyll profile is conveniently determined by a specified surface value $[\text{Chla}]_{\text{surf}}$. Because of the non-zero slope s, at some depth the formulas above will result in negative [Chla] values. When this happens, we just reset the [Chla] value at that depth to be zero. Figure 2 shows the vertical [Chla] profiles for a set of $[\text{Chla}]_{\text{surf}}$ values: 0.03, 0.1, 0.3, 1.0, and 3.0 mg/m^3, which are used in the following simulations.

The procedure to determine the Raman excitation wavelength range is described in [47]. For FDOM and chlorophyll fluorescence simulations, the excitation wavelength range is specified by Eqs. (8) or (11). A spectral resolution of 10 nm is used to ensure accuracy while maintaining efficiency [46]. Once all the radiation fields at the excitation wavelengths are finished, a final elastic vector radiative transfer simulation is performed with the inelastic source included. In

Optics EXPRESS

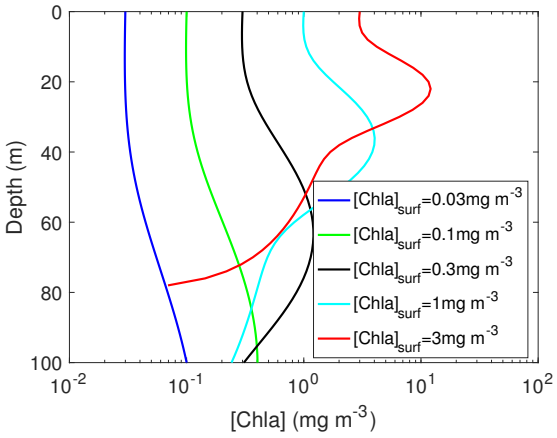

Fig. 2. Chlorophyll concentration profile for a set of $[\text{Chla}]_{\text{surf}}$ values

the following results, the water column depth is fixed at 100 m with detectors evenly placed in the water column. This large depth leads to very large optical depths at some wavelengths due to large ocean water absorption coefficient. This is the reason that it takes around 30 minutes on average to simulate the angular and depth resolved inelastic scattering contribution at an emission wavelength with the gfortran compiler 5.0 an AMD Opteron(TM) 6386 SE Processor.

The solar zenith angle is 45 degrees and the wind speed is 5 m/s. The emission wavelengths are 412, 443, 490, 555, 665, 670, 675, 680, 685, 690 nm, in which those shorter than 670 nm are typical wavelengths used for ocean color remote sensing, while those longer than 670 nm are added to study the sensitivity of chlorophyll a fluorescence. We realize that there are some water vapor absorptions in those longer wavelengths, which is likely to change the relative magnitude of elastic and inelastic scattering signals. For the wavelengths of 680, 685, and 690 nm, we have calculated the water vapor transmission for a typical tropical atmospheric column, which represents an atmospheric condition with large water vapor absorption. A spectral filter of 2 nm resolution is used to smooth out the transmission spectra. The Atmospheric Radiative Transfer Simulator (ARTS) [75] is used for the calculation with the molecule absorption line parameters provided by the high-resolution transmission molecular absorption database (HITRAN) [76]. It is estimated that the column transmission due to water vapor absorption at 680, 685, and 690 nm are smaller than 1%, which should not pose any noticeable impacts to the simulations presented in this paper. Recall that the focus of this study is the inelastic scattering in ocean waters and their contribution to the underwater polarized radiance field.

4.1. Radiance field

Figure 3 shows the inelastic scattering contribution to the total radiance field as a function of wavelength for a detector just below the ocean surface. The left column shows the absolute reflectance contribution $L_{F,u,0^-}/E_{t,0^-}$, where L is the radiance, the same quantity as I in the Stokes parameter; $E_{t,0^-}$ is the downwelling irradiance with 0^- shows the location of the detector, which is just below the ocean surface; and, subscript t stands for "total" radiation field; the subscript F can be either R, Y, or C, standing for Raman, FDOM, and or chlorophyll fluorescence; the subscript u denotes the upwelling radiance with the viewing zenith angle of zero. The right column shows the percentage fraction of inelastic scattering in the total upwelling nadir-viewing radiance $100 \cdot L_{F,u,0^-}/L_{t,u,0^-}$.

Figure 3(a) shows that the Raman scattering reflectance peak location shifts from 490 nm to

Optics EXPRESS

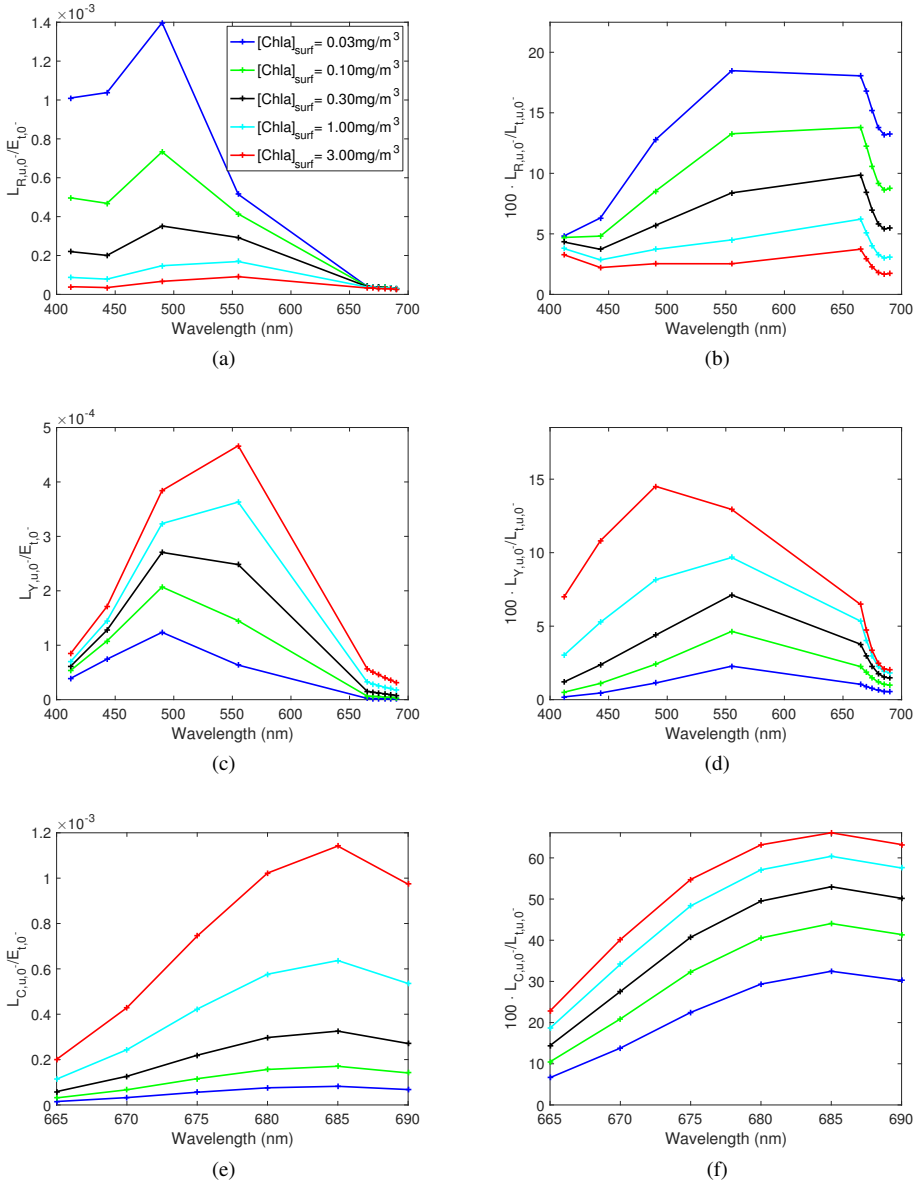

Fig. 3. Absolute and relative inelastic scattering contribution to a detector just below the ocean surface for a set of $[Chla]_{surf}$ values. The Y-axis labels denote the different quantities plotted. The subscript R, Y, and C denotes Raman, FDOM, and chlorophyll fluorescence, respectively. The legend in Fig. 3(a) applies to all figures in Fig. 3. Note the different wavelength range in Figs. 3(e) and 3(f).

555 nm as the $[Chla]_{surf}$ value increases. Figure 3(b) is similar to Fig. 3b in [47], except that the total radiance now includes FDOM and chlorophyll fluorescence. Raman scattering reflectance decreases as wavelength increases after the spectral peak. However, the percentage fraction remains largely flat because the total radiance field also decreases at similar rates. Consistent with the cases reported in [47], Raman scattering contributions decrease as $[Chla]_{surf}$ increases. The spectral trough centered at 685 nm in Fig. 3(b) is due to the large chlorophyll fluorescence contribution in that wavelength range, which can be observed in Figs. 3(e) and 3(f).

The spectral shape of the fractional contribution in Fig. 3(d) is similar to the semianalytical results shown in [49]. The order of magnitude is also consistent with the model result in [48] (See Fig. 3 of [48]). The absolute contribution in Fig. 3(c) largely resembles the spectral shape of Eq. (7) for sample HA7 reported in [49]. These observations confirm that our implementation is consistent with the physics and generates reasonable results. The FDOM absolute contribution increases as $[Chla]_{surf}$ increases, with the largest contribution around 500 nm. The relative fraction ranges from 0 to 15% depending on the wavelength and $[Chla]_{surf}$ values. Figure 3 indicate the contribution of Raman scattering is larger than that of FDOM in the visible for $[Chla]_{surf}$ <1 mg m^{-3}.

For the selected wavelengths, the contribution of chlorophyll fluorescence is significant only at wavelengths between 665 nm and 690 nm. Figures 3(e) and 3(f) show that the chlorophyll fluorescence spectral shape is a Gaussian (see Eq. (12)) centered at 685 nm. The percentage fraction increases as $[Chla]_{surf}$ increases. The peak value changes from 30% for $[Chla]_{surf}$ =0.03 mg/m^3 to more than 60% for $[Chla]_{surf}$ =3 mg/m^3. This indicates that the chlorophyll fluorescence band centered at 685 nm can be a source of information for ocean productivity remote sensing.

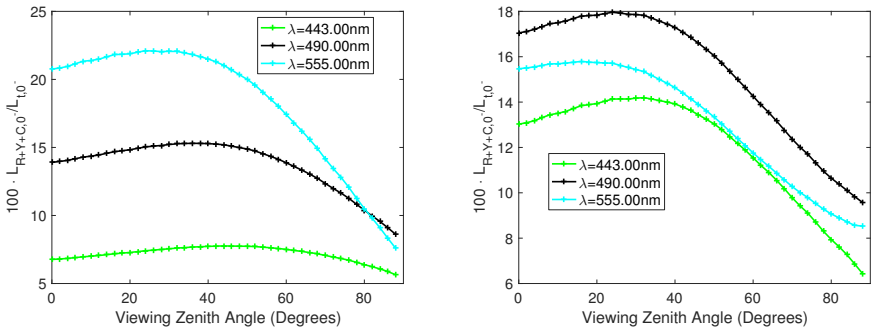

(a) $[Chla]_{surf}$ =0.03 mg m^{-3} (b) $[Chla]_{surf}$ =3 mg m^{-3}

Fig. 4. Fraction of inelastic scattering just below the ocean surface as a function of viewing zenith angle in the principal plane.

Figure 4 provides some sense of the angular distribution of the inelastic fraction 100 · $L_{R+Y+C,\,0^-}/L_{t,\,0^-}$ for two values of $[Chla]_{surf}$: 0.03 mg m^{-3} and 3 mg m^{-3}. The subscript R+Y+C shows all inelastic contributions, Raman scattering, FDOM, and chlorophyll fluorescence are included. The subscript t=R+Y+C+E, where E is elastic scattering. The viewing azimuth angle is zero in Fig. 4, i.e., the solar principal plane is used. Figure 4(a) shows that the inelastic fraction for $[Chla]_{surf}$ =0.03 mg m^{-3} has little angular dependence up to the viewing zenith angle of 50 degrees. Then the fractions start to drop off. The fractions at 443 nm and 490 nm show smaller angular variations than longer wavelengths at 555 nm. Figure 4(b), on the other hand, shows a larger angular variation for all wavelengths. Note that the angular variation of radiance due to inelastically scattered light should be weak. The angular variation in the inelastic fraction shown here is mostly due to the angular variation of total radiance field $L_{t,\,0^-}$, which is highly

dependent on the phase function, and single scattering albedo for the scattering medium. We have also confirmed that the azimuth viewing angle dependence of the inelastic fraction is very weak (plot not shown). The overall angular dependence of the inelastic scattering is smooth and limited as indicated by Fig. 4.

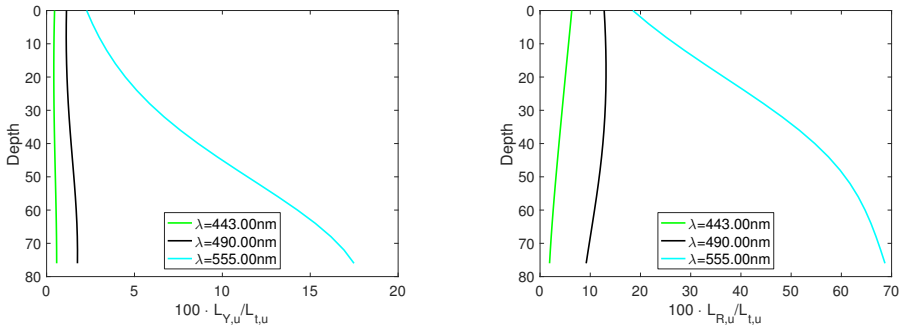

(a) $[Chla]_{surf}$ =0.03 mg m^{-3} (b) $[Chla]_{surf}$ =0.03 mg m^{-3}

(c) $[Chla]_{surf}$ =1.0 mg m^{-3} (d) $[Chla]_{surf}$ =1.0 mg m^{-3}

Fig. 5. Fraction of CDOM fluorescence and Raman scattering at nadir as a function of detector depth.

Figure 5 shows the FDOM and Raman inelastic contribution fraction as a function of detector depth in water for three wavelengths. In Fig. 5, subscript u indicates the radiance is for nadir-viewing. For a small value of $[Chla]_{surf}$ =0.03 mg m^{-3}, the FDOM fraction $100 \cdot L_{Y,u}/L_{t,u}$ has small changes as the detector depth is larger, for wavelengths shorter than 490 nm. The fractions, however, increase rapidly for the wavelength of 555 nm, with the maximum fraction reaching 18 % around 70 meters. The Raman scattering fraction is larger than FDOM, but with similar trends as a function of depth and wavelength. Raman scattering contributes near 70% for λ=555 nm at 70 meters. For a large value of $[Chla]_{surf}$ =1 mg m^{-3}, the Raman scattering fraction decreases for all wavelengths as the detector goes deeper. The FDOM fraction for 490 nm and 555 nm also decreases for $[Chla]_{surf}$ =1 mg m^{-3}. This is not the case for λ=443 nm, however, which decreases first and then increases. This non-monotonic behavior exists because the rate of fractional change depends on how the absolute radiance contribution changes for all three components: elastic scattering, Raman scattering, and fluorescence. Different rates of change for the three components lead to different fractions at different detector depths.

Figure 6 shows the chlorophyll fluorescence fraction at 685 nm as a function of detector depth for five $[Chla]_{surf}$ values. For $[Chla]_{surf}$ values smaller than or equal to 0.1 mg m^{-3},

Optics EXPRESS

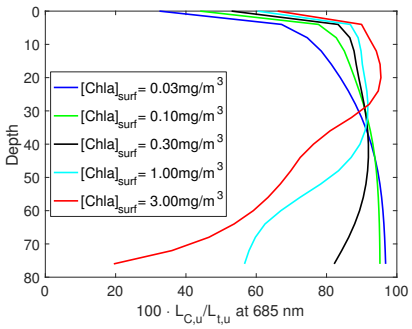

Fig. 6. Fraction of chlorophyll a fluorescence at 685 nm at nadir as a function of detector depth.

the chlorophyll fluorescence increases monotonically as detectors go deeper. For $[\text{Chla}]_{\text{surf}}$ values larger than 0.1 mg m^{-3}, the chlorophyll fluorescence fractions first increase and then decrease after they reach peak at depth. The reason is that a larger $[\text{Chla}]_{\text{surf}}$ value leads to more fluorescence at shallow water depths. However, a larger $[\text{Chla}]_{\text{surf}}$ value also causes larger extinction coefficients at excitation wavelengths. As a consequence, the excitation radiation attenuates faster, which induces less fluorescence at deeper water depths. It is also observed from Fig. 6 that the fluorescence fractions change at different rates at different depths. This is because radiances from these different sources, elastic, Raman, and fluorescence monotonically decrease at different rates. The different rates of change for these radiances have led to the chlorophyll fluorescence fraction changes at different rates.

4.2. *Polarized features*

A special feature of this work is that the fluorescence is built in a fully polarized radiative transfer model. Thus we can study the impacts of the inelastic scattering to the polarized radiation field. The Degree of Linear Polarization (DoLP) is an important parameter to study polarized radiation field:

$$\text{DoLP} = \sqrt{\text{Q}^2 + \text{U}^2}/\text{I}. \tag{25}$$

Figure 7 shows DoLP at 685 nm as a function of viewing angles for two different detector locations. Figures 7(a) and 7(c) are the DoLP originating from elastic scattering only; and Figs. 7(b) and 7(d) are the DoLP originating from all the sources, including both elastic scattering and inelastic scattering. The colorbar in Fig. 7 shows the value of DoLP. The semicircles show the viewing angle plotted in polar coordinate. For an arbitrary pixel in the semicircle, the distance between the pixel to the origin (center of the semicircle) is the viewing zenith angle; the angle between the positive x-axis (from the origin to the right) and the line segment connecting the pixel and the origin is the viewing azimuth angle. The values of the viewing azimuth angles are shown by the bold numbers around the semicircle; while the viewing zenith angle is shown by the numbers along the positive x-axis.

Figure 7 shows that the angular distribution of DoLP is similar for all the cases, with a minimum value of near zero centered at the backscattering direction of solar light direction refracted by the water surface. The maximum values vary and are distributed in an arched area which has the scattering angle of 90°, a feature determined by the single scattering reduced Mueller matrix [65]. For elastic scattering, the peak value of DoLP decreases as detector depth increases. For DoLP including both inelastic and elastic scattering, the angular pattern is similar. However, DoLP is greatly reduced due to inelastic scattering as fluorescence is completely

Optics EXPRESS

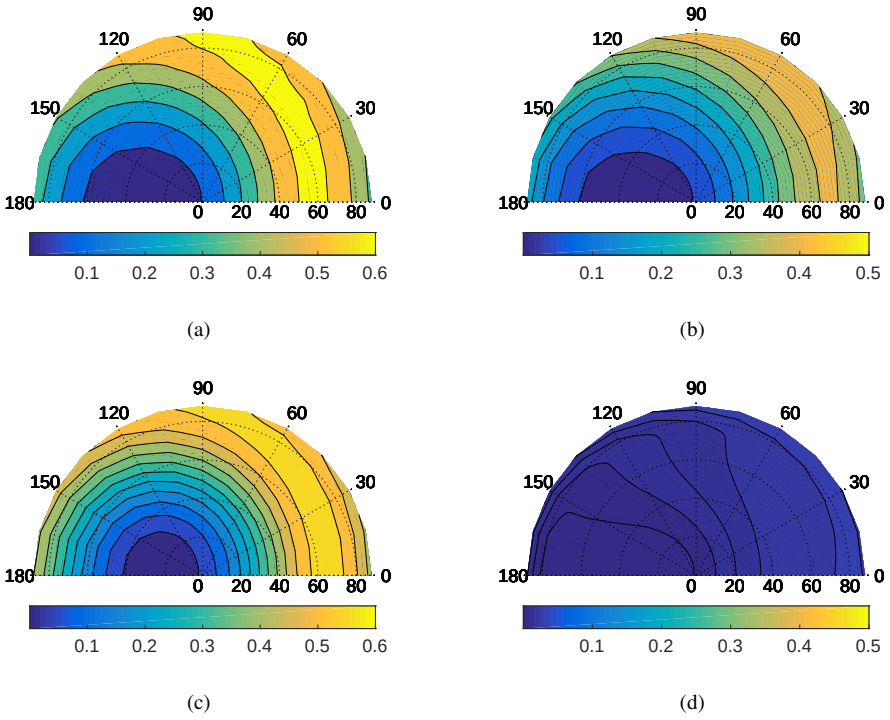

Fig. 7. Angular distribution of DoLP at 685 nm for elastic scattering and total (elastic + inelastic) scattering at two different detector locations. $[Chla]_{surf}$ =0.1 mg m^{-3}. (a) Elastic scattering for a detector just below ocean surface. (b) Total scattering for a detector just below the ocean surface. (c) Elastic scattering for a detector 30 meters below the ocean surface. (d) Total scattering for a detector 30 meters below the ocean surface.

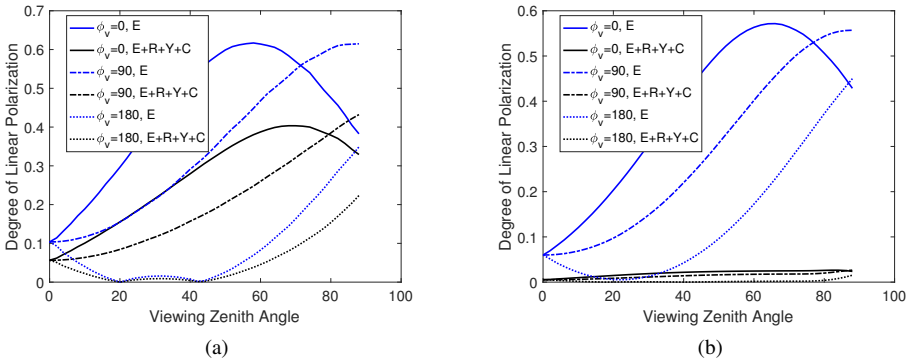

Fig. 8. DoLP at 685 nm as a function of viewing zenith angle for three azimuth plane at two different detector locations. $[Chla]_{surf}$ =0.1 mg m^{-3}. (a) Detector just below ocean surface. (b) Detector 30 m below ocean surface

unpolarized and Raman scattering generally results in smaller polarization [47]. For the detector located 30 meters below the surface, the radiation field originated from the elastic scattering is still highly polarized. When we include inelastic scattering, the polarization feature is almost completely neutralized. The magnitude of DoLP reduction is consistent with Fig. 6, in which the fluorescence contribution at 685 nm accounts for about 90% of the signal at 30 m below the water surface.

To better show the magnitude of DoLP, Fig. 8 shows DoLP as a function of viewing zenith angle for three different azimuth plane 0°, 90°, and 180°. Elastic scattering is denoted as "E" without any subscript. Earlier in this paper E has been used to denote irradiance which is always accompanied with subscripts to denote detector locations and sources. Total scattering is shown as "E+R+Y+C", which include contributions from all scattering sources. For the detector just below the ocean surface, the change due to inelastic scattering is around 0.05 for nadir viewing direction. This change is a function of viewing geometry and can be as large as 0.3. For the detector 30 meters below the ocean surface, the DoLP due to elastic scattering is only slightly less than the DoLP near the surface. However, it is almost uniformly close to zero for the detector 30 meters below the surface. DoLP has been related to water single scattering albedo [77]. The result shown in Fig. 8 indicates that the impacts of inelastic scattering on DoLP are large and should be taken into account when extending remote sensing algorithms using DoLP into wavelengths with strong inelastic scattering.

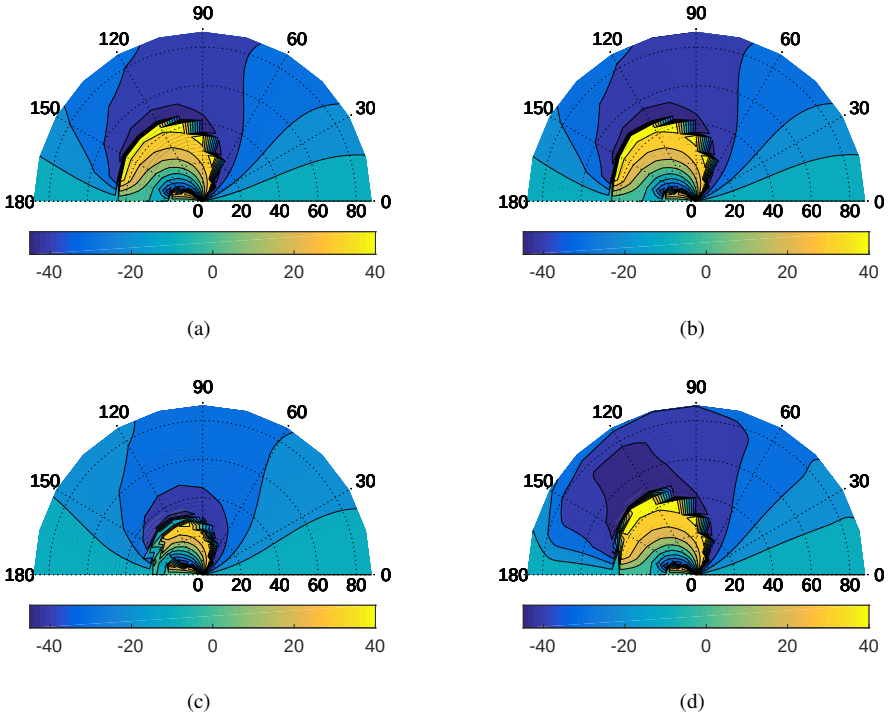

Fig. 9. Angular distribution of the orientation of the polarization ellipse (OPE) for elastic scattering and total (elastic + inelastic) scattering at two different detector locations. $[Chla]_{surf}$ =0.1 mg m^{-3}. (a) Elastic scattering for a detector just below ocean surface. (b) Total scattering for a detector just below ocean surface. (c) Elastic scattering for a detector 30 meters below the ocean surface. (d) Total scattering for a detector 30 meters below the ocean surface.

Optics EXPRESS

The impacts of inelastic scattering to the orientation of the polarization ellipse (OPE) is studied in Fig. 9. In this work the OPE is defined as:

$$\mathrm{OPE} = \frac{\arctan\left(\mathrm{U/Q}\right)}{2}, \tag{26}$$

which means that we do not adjust the angle to be within 0 and 180° in order to avoid numerical instability as Q could be zero. The layout of Fig. 9 is the same as Fig. 7, except that the OPE is plotted. If only elastic scattering is included, the OPE just below the ocean surface shows a positive region near backscattering direction of the solar incident light. It then transits from positive to negative around zenith angles between 20° to 40°, indicating a sign change of U/Q. For the detector 30 m below the surface, the positive region is confined in a smaller cone, approximately within 20° of the viewing zenith angle. When inelastic scattering is taken into account, the OPE near the surface shows a similar pattern to the elastic figure. However, the OPE angular pattern at 30 m below the surface is different from the one with elastic scattering only. The main difference is the angular range of the positive values of OPE. The subtle difference of OPE between elastic scattering and total scattering fields reflects the interaction between elastic scattering and less polarized inelastic scattering, which demonstrates the value of this work.

5. Conclusion

A full-physical radiative transfer model has been developed for coupled atmosphere and ocean systems, which treats polarization exactly and includes both elastic and inelastic scattering. In inelastic scattering, Raman scattering, FDOM and chlorophyll fluorescence are included. Sensitivity studies were performed to evaluate the impacts of inelastic scattering on the polarized radiation field in case 1 ocean waters. Chlorophyll fluorescence was shown to have negligible contributions to the total radiation field in the visible, except in a narrow band center at 685 nm. For relatively clear waters ($[\mathrm{Chla}]_{\mathrm{surf}}$ <1 mg m^{-3}), Raman scattering was shown to have a larger contribution to the total radiation field than the FDOM. This comparison of Raman scattering and FDOM signals is however based on the bio-optical model used for Case 1 waters. The result for Case 2 waters are likely to be different, which is of interest for a future study. The FDOM fraction was shown to be small at the two spectral ends of 412 nm and 690 nm, and larger in the middle with peak around 555 nm, which is determined by the emission function of [49] used in this work. The angular distribution of the inelastic scattering fraction was found to be smooth and limited. At different depths, the fractions of different inelastic scattering sources varied in a large range, from 0 to nearly 100 %, depending on the depth, wavelength, and water turbidity. The inelastic scattering contributions were found to have apparent impacts on the underwater DoLP. These effects are most significant at 685 nm where chlorophyll fluorescence peak is located. Inelastic scattering played a smaller role to OPE angular distribution. However, for a detector at depth, the OPE difference between elastic and inelastic scattering was noticeable. This reflects the complicate compound effect of the inelastic scattering to the polarized radiation field. This work is critical for understanding the underwater polarized radiation field impacted by a set of interacting scattering sources, and can ultimately be used to develop new remote sensing algorithms for ocean color based on polarimetry.

Funding

NASA Grants (NNX15AB94G, NNX15AK87G).

Acknowledgments

Pengwang Zhai is partially supported the NASA PACE Project. This study is also partially supported by the NASA Radiation Science program administrated Hal Maring and the Biology and Biogeochemistry program administrated by Paula Bontempi.